SUPERVISED MACHINE LEARNING ALGORITHMS FOR EARLY DETECTION OF ORAL EPITHELIAL CANCER USING FLUORESCENCE LIFETIME IMAGING MICROSCOPY

A Thesis

by

JOOHYUNG LEE

Submitted to the Office of Graduate and Professional Studies of
Texas A&M University
in partial fulfillment of the requirements for the degree of

MASTER OF SCIENCE

Chair of Committee,	Jim Ji
Co-Chair of Committee,	Javier Jo
Committee Members,	Raffaella Righetti
	Sebastian Hoyos
Head of Department,	Chanan Singh

August 2014

Major Subject: Electrical Engineering

ABSTRACT

In this study, the clinical potential of the endogenous multispectral Fluorescence lifetime imaging microscopy (FLIM) was investigated to objectively detect oral cancer. To this end, *in vivo* FLIM imaging was performed on a hamster cheek pouch model with an oral epithelial cancer. The autofluorescence emissions of the hamster tissue were recorded in three different spectral bands which were determined based on the peak emission wavelength of three major fluorophores of hamster mucosal tissue: collagen (390±20 nm), NADH (452±22.5 nm), and FAD (>500 nm). Then, a total of 7 features pertaining to FLIM were extracted from each channel, providing 21 features overall.

To design a classifier in a supervised approach, a training set is required, in which each pixel is labeled with one of the four groups. In this study, we utilized a total of 65 regions of interest (ROI) from the imaged cheek pouch of seven hamsters, for which the histopathological diagnosis could be correlated. The resulting database was used to train a K-Nearest-Neighborhood (KNN) algorithm aimed to detect benign from pre-malignant/malignant lesions. In addition, a Sequential Floating Forward Selection (SFFS) was applied to optimize the KNN algorithm and identify a subset of features that would maximize the classification performance. The best performance corresponded to the 3-NN algorithm with the $\frac{1}{e}$ lifetime in the NADH channel and the normalized intensity in FAD channel as features. The overall accuracy, sensitivity and specificity for detecting pre-malignant and malignant lesions were 92.2%, 87.3%, and 94%, respectively, assessed using a cross-validation method. It has to be noted that the feature

selection algorithm suggested both lifetime parameter and intensity parameter for an optimal feature set, which validates the need to utilize endogenous FLIM for the objective detection of oral cancer. At last, all data from the 65 ROIs were used to train the 3NN classifier to classify the full tissue areas. The results suggest that multispectral endogenous FLIM has a potential to screen malignant oral epithelial tissue. This technology, however, still needs to be evaluated in human patients.

DEDICATION

To all of my hope forever, Christ Jesus

ACKNOWLEDGEMENTS

I would like to deeply thank my committee chair Dr. Ji and my committee co-chair, Dr. Jo who have guided and supported me as fathers in my academic career. I also want to thank my committee members, Dr. Righetti, who truly cares about her students, and Dr. Hoyos for their support throughout the course of this research.

Special thanks to Dr. Malik, Dr. Paritosh, Michael, Ms. Tammy, Ms. Jeanie, my colleagues, and Texas A&M University, who have not only helped me pursue my academic goal but also shared invaluable memories with me.

Finally, thanks to my father and my mother who love me more than anything; my Aggie brother, grandparents, all of my friends, and my family members for their encouragement and support.

NOMENCLATURE

FLIM	Fluorescence Lifetime Imaging Microscopy
RCM	Reflectance Confocal Microscopy
IRF	Impulse Response Function
UV	Ultraviolet
NIR	Near Infrared
$\frac{1}{e}$ lifetime	$\frac{1}{e}$ lifetime
cc	Laguerre Coefficient
cc_norm	Normalized Laguerre Coefficient
I_k	Intensity in channel k
In	Normalized Intensity
In_k	Normalized Intensity in channel k
SNR	Signal-to-Noise Ratio
HGD	High-Graded-Dysplasia
LGD	Low-Graded-Dysplasia
Ch	Channel
N/A	Not Available

TABLE OF CONTENTS

Page

LIST OF FIGURES

Page

LIST OF TABLES

Page

CHAPTER I

INTRODUCTION

In 2013, over 8,000 people in the United States have died from oral or pharyngeal cancer, and more than 42,000 patients have been newly diagnosed [1]. The 5-year survival rate of oral cancer is approximately 80% when it is diagnosed while the disease is still localized; however, only around 30% of patients are diagnosed at this early stage [1]. The 5-year survival rate drops to approximately 50% once the cancer has already spread to adjacent oral tissues or lymph nodes, and almost 50% of patients are diagnosed at this stage [1]. The 5-year survival rate falls below 30% once the cancer has spread further to distant organs [1]. Furthermore, while the early stage of oral cancer treatment may only demand minor treatment on the localized tumor, later stage treatment could involve surgery to remove parts of the lip, tongue, jaw, or neck [1]. In addition, around 30% of the patients who survived after the first incidence will suffer from a recurring cancer [1]. Consequently, early detection of oral cancer includes newly developed cancer as well as the recurrent cancer.

Usually, early detection of oral cancer is hinged on the health provider's individual ability to recognize the subtle changes towards pre-malignant lesions and cancers from alterations towards inflammatory benign conditions which possess the majority of mucosal abnormalities [2]. As a consequence, the individual ability of the clinicians in making such judgments is critical [2]. Once the need to biopsy has been suggested, another important challenge arises; to decide where to biopsy the identified

lesions [2]. This becomes more important when the lesions are ill-defined, or if the cancer is widely spread across the mucosa [2]. Such situations are challenging even for experienced professionals [2].

A further area of concern involves the demarcation of surgical margins which are expected to include all high-risk tissue [2]. Usually, if anatomically feasible, a 10 mm normal-looking oral mucosa borders around the clinically cancerous lesion are removed [2]. However, carcinoma often recurs where it has appeared before, and it indicates the limitation of the current practice [2].

Finally, follow-up of patients after treatment is hard [2]. Clinical examinations often gets complicated when the cancer recurs where it has been treated already since it is hard to recognize pre-malignant or malignant alteration in such case [2]. To these patients, repeated comparative biopsies are impractical [2]. There are several tools which fall under one of the following three categories: vital staining, exfoliative cytology, or optical imaging [3-13]. However, unfortunately, their performance as diagnostic tools particularly in detecting lower-risk lesions has not been yet established, and their definition for positive diagnosis is not reliable [2]. Thus, clinical tools that can diagnose oral precancers and cancers more accurately than visual inspection alone by clinician are needed in order to guide tissue biopsy and resection.

A description of important changes of biochemical and functional biomarkers associated to oral epithelial cancer progression is provided in Figure 1. The diagnostic competence of autofluorescence imaging and spectroscopy comes from the ability to noninvasively probe subtle neoplastic alterations that occur during malignant

progresssion [14]. Fluorescence in epithelial tissue comes from multiple fluorophores and is influenced by absorption and scattering as light propagates through the epithelium and stroma [1, 15, 16]. Both mitochondrial metabolic coenzymes flavin adenine dinucleotide (FAD) and the reduced form of nicotinamide adenine dinucleotide (NADH) in the epithelial cells as well as collagen-cross links in the underlying stroma have been identified as the dominant sources of autofluorescence when the tissue is excited by the ultraviolet light [1, 17]. In addition, neoplastic progression also incurs change in the amount of both FAD and NADH as well as increase in the epithelial nuclear size, chromatin texture, and concentration of epithelial nuclei which induce more frequent epithelial scattering [1].

In particular for the detection of an oral cancer, the autofluorescence signal from both NADH and FAD increases as dysplasia develops whereas it decreases in inflammatory benign condition [17]. Such phenomenon allows the benign and precancerous lesions to be easily differentiated. However, the overall tissue fluorescence intensity generally decreases in both cases [17]. It is because the overall fluorescence is dominated by the stromal fluorescence, which decreases in both benign and precancerous lesions [17]. Consequently, the autofluorescence signals from stromal collagen needs to be separated from the autofluorescence emissions from both NADH and FAD in order to distinguish benign and precancerous lesions [17]. In this study, therefore, the fluorescence signals from collagen, NADH, and FAD are recorded separately in three different channels by considering the emission peak spectra of collagen, NADH, and FAD.

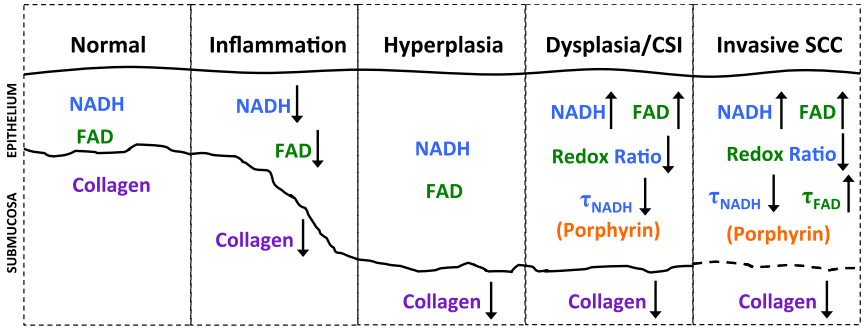

Figure 1 Summary of relevant endogenous biochemical and functional biomarkers associated to oral epithelial cancer progression.

Traditionally, fluorescence microscopy has mainly been implemented in steady-state analysis such as overall intensity or peak wavelength, which reveals the fluorescence responses as a function of excitation wavelength [18, 19]. This approach has been widely examined for clinical application [20]. However, this method is sensitive to various intensity-based artifacts which are hard to control during clinical procedures [19]. Such artifacts include fluorophore concentration, probe to tissue distance, excitation source intensity, etc [19]. On the other hand, lifetime which represents the average time that the molecule remains in the excited state before returning to the ground state, is less sensitive to such artifacts [20, 21].

As a result, fluorescence lifetime imaging microscopy (FLIM) can definitely improve the analytical quality of the neoplastic progression of the tissue [22]. The lifetime information of both FAD and NADH vary with the metabolic state of the tissue and thus provide distinction between different stages of dysplasia, which can be

additional means for detecting highly active premalignant tissue [22]. Furthermore, such approach can better characterize the tissue with fluorophores of heavily overlapping emission spectra [23]. Table 1 shows that the lifetime not only provides distinctive values for fluorophores with overlapping spectra such as NADH and collagen but also is sensitive to local microenvironment of the tissue, which enables to probe the malignant transformation of the lesion [17, 24].

FLIM can be performed either in frequency domain or in time domain [25]. Though frequency domain FLIM has the advantage of simpler instrumentation, it shows its limitation on analysis of a complex signal [25]. Time domain FLIM, however, is more suitable for studying a variety of FLIM signals, though it is more demanding in terms of experimental setup [25]. In time domain setup, the tissue is excited with the pulsed laser pixel-by-pixel. At each pixel, the fluorescence emission is recorded over time. Then, the deconvolution algorithm estimates the IRF at each pixel. Finally, the decay rate of the IRF is quantified in two different variables: $\frac{1}{e}$ lifetime and average lifetime.

The goal of this thesis was to demonstrate the potential of endogenous multispectral FLIM for detecting and distinguishing benign from pre-malignant and malignant oral epithelial tissue in a hamster cheek pouch model of oral epithelial cancer.

Table 1 Relevant endogenous fluorophores in epithelial tissue

Fluorophore	Excitation (nm)	Emission (nm)	Lifetime (ns)
Collagen	350	390	3-5
NADH	350	460	0.5/1-3 (free/bound)
FAD	450	550	2-3/1 (free/bound)
Porphyrin	400	630	>9

CHAPTER II

METHODOLOGY

2.1 Tissue Sample Preparation

To perform the *in vivo* imaging of premalignant oral mucosal tissue, seven hamster cheek-pouch models of oral cancer were imaged. In a pathogen-free house, the hamsters were fed rodent chow and water *ad libitum* [17]. To induce the oral carcinogenesis at the Golden Syrian hamster pouches, 7; 12-dimethylbenz[α]anthracene (DMBA) was used [17]. The animal-use protocol was reviewed and approved by the Texas A&M University Institutional Animal Care and Use Committee (IACUC), whereas the clinical aspect of the study was supervised by veterinarians [17].The procedure to prepare and to image the early stage of oral carcinogenesis has been presented by Jabbour et al, which is discussed as follows [17].

The right buccal pouch of each hamster served as a cancer tissue whereas the left pouch worked as a normal tissue [17]. The right pouch of each hamster was treated with 0.5% DMBA solution (Sigma-Aldrich) dissolved in mineral oil (Sigma-Aldrich); the left pouch of each hamster was treated with mineral oil only [17]. Both the right and the left pouches of each hamster were treated 3 times a week for 8 weeks [17]. At the time of imaging, 10% urethane solution was intraperitoneally injected in order to anesthetize each hamster [17]. Then, the cheek pouch was pulled and clamped onto the custom built mount for maximum exposure of the tissue area [17]. In addition, the hamster was kept warm with a heating pad so that the exposed cheek pouch was likely between room

temperature and the body temperature of the hamster [17]. After imaging of the buccal mucosa, the pentobarbital solution was injected into each hamster to euthanize it [17]. The cheek pouches were then excised and fixed in 10% formalin to be processed for H&E histology [17].

2.2 Histology Analysis

Initially, a goal of this study was to classify each image pixel into one of the four histopathological groups: cancer, benign, low-graded-dysplasia (LGD), and normal. To design a classifier in a supervised approach, a training set is required, in which each pixel is labeled with one of the four groups. In this study, the training set is constraint to the data from a total of 65 regions of interest (ROI) from seven hamster cheek pouch models. More specifically, onlyA total of 65 regions of interest (ROI) in the FLIM images could be correlated with the underlying tissue histopathology. Each ROI was 11×11 pixels in size (0.44mm×0.44mm) and was classified as: normal, cytologic atypia, hyperplasia, hyperkeratosis, low-graded-dysplasia (LGD), high-graded-dysplasia (HGD), or squamous cell carcinoma (SCC). Cytologic atypia, hyperplasia, hyperkeratosis were combined into a benign group. All HGD and SCC lesions were combined into a cancer group. Among 65 ROIs, 17 ROIs are classified as cancer, 12 as LGD, 17 as benign, and 19 as normal. In addition, in this paper, seven hamster cheek pouch models will be identified by sequential numbers: 1 through 7.

2.3 Fluorescence Lifetime Imaging System

A detailed schematic of the large-field FLIM system is illustrated in Figure 2 and described in a previous publication. Since ultraviolet light excitation can effectively excite the endogenous fluorophores present in epithelial tissue, the system employs a UV frequency-tripled Q-switched ND:YAG laser (1 ns pulse-width, 355 nm, 100 kHz maximum repetition rate, AOT-YVO-100QSP/MOPA, Advanced Optical Technology, Essex, United Kingdom) for excitation [1, 17]. The light from the laser is transmitted into the high –OH silica core multimode fiber (FVP050055065, Polymicro Technologies, Phoenix, Arizona) with a diameter of 50 μm [17]. To correlate the input excitation with the resulting fluorescence decay curve, some of the light from the laser transmits into the photodiode as well [17]. A dichroic mirror (DM1, NC176741-z355rdc, T > 95% for 380 to 800 nm, Chroma Technology Corporation, Bellows Falls, Vermont) collimates, reflects, and then forwards the ray from the fiber to a pair of close-coupled galvanometer mirrors (6200HM40, Cambridge Technology, Lexington, Massachusetts) for two-dimensional raster scanning, which divides the whole tissue sample area into 388×400 pixels [17]. Then, the light is focused onto the sample by a UV-to-NIR corrected triplet lens (NT64-837, Edmunds Optics, Barrington, New Jersey) with a focal length of 45 mm and effective numerical aperture (NA) of 0.06 [17].

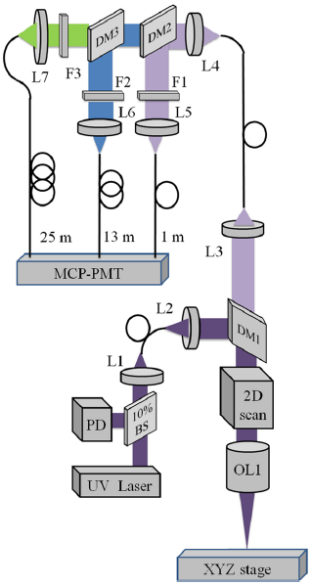

Figure 2 Schematic of the combined fluorescence lifetime imaging [17]

The fluorescence emission from the sample propagates through the same triplet lens and then is separated from the laser light by DM1 [17]. After being separated, the emission from the sample is coupled into a multimode fiber with a core diameter of 200 μm (BFL22-200, Thorlabs, Newton, New Jersey) [17]. Two dichroic mirrors (DM2, LM01-427-25, T > 95% for 439 to 647 nm, and DM3, FF484-Fdi01,T > 95% for 492 to 950 nm, Semrock, Rochester, New York), two bandpass filters (FF01-390/40, FF01-452/45, Semrock), and a long pass filter (FF01-496, Semrock) split the light from the fiber into the rays of three different spectral bands, which were determined based on the emission spectra of the three endogenous fluorophores of interest: collagen (F1: 390±20 nm), NADH (F2: 452±22.5 nm) and FAD (F3: >500 nm) [17].

To consecutively record the three different signals with one detector, different time delays were applied to each of these three rays of different spectral bands [17]. These three rays are coupled into the three multimode fibers with lengths of 1, 13, and 25 m (BFL22-200, Thorlabs), creating a time delay of 60 ns between two rays of consecutive spectral bands [17]. Finally, a high-speed (180 ps rise time, 90 ps TTS) micro-channel plate photomultiplier tube (MCP-PMT, R5916U-50, Hamamatsu, Bridgewater, New Jersey) collects the three decays consecutively in 200ns [17]. The collected signals are then sampled by a digitizer at 6.25 GHz (PXIe- 5185, National Instruments, Austin, Texas) after being amplified by the preamplifier (C5594- 12, Hamamatsu) [17]. The sampling was carried out by a custom algorithm, built with LabVIEW (National Instruments) [17]. The maximum noise level of the FLIM system was verified to be negligible by imaging a mirror placed on the FLIM focal plane [17].

2.4 Laguerre Deconvolution Method

In the context of time-domain FLIM, the measured fluorescence intensity decay data y(n) is given by the convolution of the fluorescence Impulse Response Function (FIRF) h(n) with the instrument response x(n):

$$y(n) = T \times \sum_{m=0}^{K-1} h(m)x(n-m), n = 0, \dots, N-1 \quad (1)$$

The parameter K determines the time length of the FIRF, T is the sampling interval, and N is the number of samples measured in y(n) and x(n). In the context of CT-TE, sampling, $N = 2^Q$. The LDM expands FIRF on an orthonormal set of Discrete Laguerre Functions (DLF): c_j^{α}h(n) = T$\times \sum_{j=0}^{L-1} c_j^{\alpha} b_j^{\alpha}(n)$, where c_j^{α}, are the Laguerre

Expansion Coefficients (LEC), which are to be estimated from the input-output data; $b_j^{\alpha}(n)$ denotes the order orthonormal DLF; and *L* is the number of DLFs used to model the FIRF (usually L<10) (38). The Laguerre parameter α ($0 < \alpha < 1$) determines the rate of asymptotic decline of the DLFs. The larger the α, the longer the spread over time of a DLF. Thus, larger α values imply longer convergence time to zero. The convolution equation can be expressed as: $y(n) = \sum_{j=0}^{L-1} c_j^{\alpha} b_j^{\alpha}(n)$, where $v_j^{\alpha}(n) = \sum_{i=0}^{K-1} b_j^{\alpha}(m)x(n-m)$. The convolution equation represents a system of linear equations on the coefficients c_j^{α}, which can be solved by linear least-square estimation. Once the coefficients c_j^{α} have been calculated, $h(n)$ can be computed and values for average lifetimes can be calculated as: $\tau = \frac{T \times \sum_{n=0}^{N} n \times h(n)}{\sum_{n=0}^{N} h(n)}$.

Dabir *et al* have previously recommended the use of four or five Laguerre bases for computational efficiency, and therefore Laguerre functions with an order of one to four will be utilized in this study [20]. Furthermore, an optimal value for the Laguerre parameter alpha can be estimated by implementing a gradient method, with its step size determined by simple bisection method [26].

2.5 Feature Retrieval and Data Preparation

The FLIM system records the autofluorescence signal with three distinct channels, and each channel is aimed to record the autofluorescence emission from one of three major fluorophores of interest: collagen, NADH, and FAD. From each channel, seven features are extracted either from the FLIM signal or from the estimated impulse response function h(n). Since there are three channels, there will be 21 features. Consequently, 21 different feature values will be assigned to each of 388×400 pixels in every tissue sample, and it generates 21 different feature maps per tissue sample. Obviously, since there are 65 regions of interest (ROI) with known histopathological classifications, each of 65 ROIs will possess 21different feature values, which will later be utilized to build a classifier for supervised machine learning. The retrieved features are: normalized intensity of the FLIM curve, four Laguerre coefficients, average lifetime, and $\frac{1}{e}$ lifetime ($\frac{1}{e}$ lifetime). The definition for each feature is presented below.

Normalized intensity is calculated directly from the FLIM decay curve. Since the FLIM signal is collected in three distinct channels, normalized intensity of a given channel is the proportional fluorescence energy of the given channel over the fluorescence energy of all three channels, which is described in equation 2. Note that "I_k" refers to the sum of the intensity over time at channel k whereas "In" refers to the normalized intensity which can be calculated by following equation.

$$In_k = \frac{I_k}{I_1+I_2+I_3} \tag{2}$$

The Laguerre coefficients, which are the coefficients of Laguerre bases, have been measured by solving a least square problem [26]. As stated in the previous section,

its detailed procedure has been presented by Pande and Jo [26]. In addition, all Laguerre coefficients, which are abbreviated as "cc", are normalized by the following equation:

$$cc\_norm_k = \frac{cc_k}{\sum_k |cc_k|} \tag{3}$$

Average lifetime for each pixel is calculated from the estimated IRF with the following equation:

$$\text{Average lifetime} = \frac{\sum_t t \times I(t)}{\sum_t I(t)} \tag{4}$$

Lifetime represents the expected time that a molecule spends in the excited state prior to return to the ground state [23]. As a result, mathematically, it can be seen as a quantity that measures the decay rate. However, there is another feature that measures the decay rate in a similar fashion, which is $\frac{1}{e}$ lifetime. For simplicity, in this paper, $\frac{1}{e}$ lifetime can be abbreviated as tau whereas average lifetime can be denoted as lifetime. The explanation of $\frac{1}{e}$ lifetime is presented below.

If the fluorescence signal at a pixel comes from a single fluorophore, the h(n) (IRF) can be modeled with a single exponential equation. In such case, the value of $\frac{1}{e}$ lifetime is same with the value of average lifetime. However, in multi-exponential IRF model, $\frac{1}{e}$ lifetime is the time when the IRF intensity equals $\frac{h(0)}{e}$ where h(t) is the IRF over time. Therefore, $\frac{1}{e}$ lifetime is another quantity that measures the IRF decay rate, and is usually shorter than the decay rate represented by average lifetime.

2.6 Statistical Analysis

One goal of this study was to classify each image pixel using the multispectral FLIM features into one of the histopathological groups defined above. To design a proper statistical classifier following a supervised approach, a training set is required, in which each pixel is labeled to one of the groups. This requirement is extremely hard to meet, since perfect co-registration between histopathology sections and FLIM maps is virtually impossible. To mitigate this problem, we restricted the training set to the pixels of the 65 ROI for which a histopathological classification was available. The capacity of the 21 FLIM features to distinguish between the histopathological classes was assessed via the following statistical analysis.

The most common statistical test to compare two distributions is the t-test. However, the two populations should be normally distributed in order to perform t-test. As a consequence, Wilcoxon rank-sum test was implemented as an alternative method. This test does not compare the individual value. Rather, it ranks all the data and compares the ranks instead of the data themselves. This method is, therefore, less sensitive to the extreme outlier in that it abates the size of the deviation by comparing the rank.

In this study, “ranksum” function in Matlab is utilized to carry out the Wilcoxon rank-sum test with training dataset from 65 ROIs. Furthermore, feature value distributions for different classifications are plotted both as boxplots and as histogram to examine which feature can distinguish which set of classifications.

2.7 Feature Selection Method with Validation Method

The statistical analysis described before allowed narrowing down the number of features that may be able to distinguish the classes of interest. With those candidate feature sets, feature selection algorithm was implemented to find the best feature subset. In this study, Sequential Floating Forward Selection method was used as a feature selection algorithm based on a performance estimation using the following.

Cross-validation all the ROIs in one animal served as a test set whereas all the other ROIs from all other animals serve as a training set to train the classifier. Since seven animals were imaged, a confusion matrix was generated from each of the seven folded cross-validations. The seven outcome matrices were then added together to produce one confusion matrix, calculated as:

$$\begin{bmatrix} TN_{Total} & FP_{Total} \\ FN_{Total} & TP_{Total} \end{bmatrix} = \begin{bmatrix} \sum_1^7 TN & \sum_1^7 FP \\ \sum_1^7 FN & \sum_1^7 TP \end{bmatrix} \quad (5)$$

Floating Search algorithm is an upgraded version of "plus-l-take-away r" algorithm. Most of the sequential search methods assume that the criterion of feature set effectiveness is monotonic [27]. More specifically, it implies that the value of the criterion function such as an error rate or sensitivity will not be degraded when adding another feature to the current feature set [27]. However, "plus-l-take-away r" algorithm deals with such problem by imposing an additional algorithm that reduces the size of the feature set. Furthermore, floating forward search algorithm brings flexibility in choosing both l and r in "plus-l-take-away r" algorithm as well as computational efficiency [27]. Error rate is the most common and legitimate criterion for feature selection and was thus used here [27]. To summarize, Sequential Floating Forward Selection algorithm can be

described in Figure 3 where "J" represents the criterion function of feature set effectiveness. Note that there are no features included initially.

SFFS Algorithm

Input:

$Y = \{y_j \mid j = 1, \ldots, D\}$ //available measurements//

Output:

$X_k = \{x_j \mid j = 1, \ldots, k, \ x_j \in Y\}, \ k = 0, 1, \ldots, D$

Initialisation:

$X_0 := \emptyset; \quad k := 0$

(in practice one can begin with $k = 2$ by applying SFS twice)

Termination:

Stop when k equals the number of features required

Step 1 *(Inclusion)*

$x^+ := \arg \max_{x \in Y - X_k} J(X_k + x)$ {the most significant feature *with respect to* X_k

$X_{k+1} := X_k + x^+; \ k := k + 1$

Step 2 *(Conditional Exclusion)*

$x^- := \arg \max_{x \in X_k} J(X_k - x)$ {the least significant feature *in* X_k

`if` $J(X_k - \{x^-\}) > J(X_{k-1})$ `then`

$X_{k-1} := X_k - x^-; \ k := k - 1$

`go to` **Step 2**

`else`

`go to` **Step 1**

Figure 3 Description on Sequential Floating Forward Selection algorithm [27]

2.8 Classification Method

The K-nearest-neighborhood (KNN) algorithm was selected as the classification method. The KNN algorithm identifies the k nearest training data points (measured in terms of the Euclidean distance) from each test data which is subject to classification. Then, the test datum is assigned to class that has the majority among k nearest data points. When k is an even number, a tie can happen. To avoid this scenario, an odd number for k is recommended. In this study, we evaluated values of k equal to 1, 3, 5 or 7.

CHAPTER III

RESULTS

3.1 Feature Estimation

Initially, 21 features were estimated either from the impulse response function (IRF) or from the fluorescence emission curve. These 21 features consist of seven features per each of three channels, which are normalized intensity, average lifetime, $\frac{1}{e}$ lifetime, four normalized Laguerre coefficients. Figure 4 shows examples of the 21 feature maps; for one of the cheek pouch imaged (denoted as tissue #2). As mentioned in section 2.4, “In”, “cc_norm”, “lifetime”, and “tau” refers to the normalized intensity, normalized Laguerre coefficients, average lifetime, and $\frac{1}{e}$ lifetime, respectively. In addition, “ch” represents channel, and therefore the three columns in Figure 4 shows the feature maps in three different channels. Furthermore, every feature map in Figure 4 displays the known regions of interest (ROIs) in tissue #2. Each box specifies the ROI location, which consists of 11×11 pixels, and the number displayed near the box is a ROI number that uniquely represents each ROI. In addition, the corresponding histopathological classification of each ROI is revealed by the color of the box; red represents cancer whereas blue indicates non-cancer. The classification algorithm was designed to distinguish only two groups: non-cancer (including normal, benign and LGD) and cancer (including HGD and SCC). A detailed definition of these histopathological classes is provided in section 2.1.

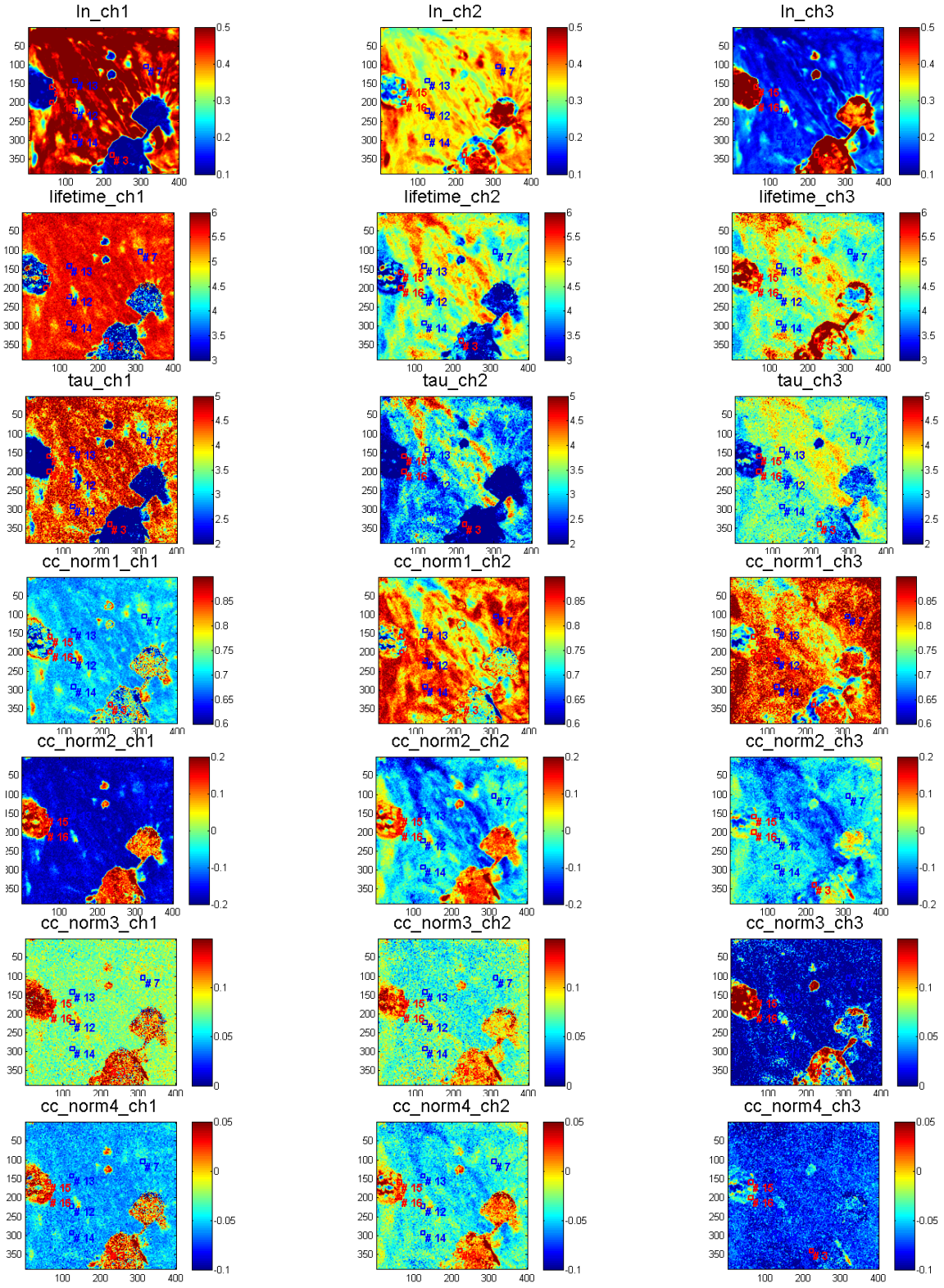

Figure 4 21 feature maps of tissue #2

3.2 Statistical Analysis

Tables 2, 3, and 4 describe the results of the ranksum test between every possible pairs of histopathological classes. The similarity between two distributions is quantified with p-value in percentage. Any pair of distributions with p-value less than one is considered significantly different, which are in bold text in the tables below.

Table 2 “p” in percentage from Ranksum Test between four classifications on Channel 1

	Channel 1					
	Cancer-Benign	Cancer - LGD	Cancer - Normal	Benign-LGD	Benign-Normal	LGD-Normal
cc_norm1	19.06	52.08	26.74	41.27	70.38	79.21
cc_norm2	**0.00**	**0.03**	**0.00**	61.06	70.38	79.21
cc_norm3	38.92	36.40	35.81	64.20	92.43	55.65
cc_norm4	**0.02**	**0.11**	**0.02**	38.79	61.22	82.35
lifetime	**0.01**	**0.07**	**0.01**	55.00	63.46	85.52
In	**0.00**	**0.01**	**0.00**	87.68	63.46	50.34
tau	**0.00**	**0.03**	**0.00**	55.00	65.73	91.92

Table 3 “p” in percentage from Ranksum Test between four classifications on Channel 2

	Channel 2					
	Cancer-Benign	Cancer - LGD	Cancer - Normal	Benign-LGD	Benign-Normal	LGD-Normal
cc_norm1	8.50	7.29	**0.71**	80.76	31.06	42.90
cc_norm2	**0.05**	**0.15**	**0.07**	64.20	39.22	52.96
cc_norm3	**0.22**	1.09	1.47	36.40	29.57	91.92
cc_norm4	**0.09**	**0.56**	**0.17**	38.79	10.61	52.96
lifetime	**0.04**	**0.21**	**0.08**	73.98	22.85	47.79
In	5.38	2.84	4.95	24.06	54.71	91.92
tau	**0.05**	**0.21**	**0.09**	49.25	29.57	61.22

Table 4 “p” in percentage from Ranksum Test between four classifications on Channel 3

	Channel 3					
	Cancer-Benign	Cancer - LGD	Cancer - Normal	Benign-LGD	Benign-Normal	LGD-Normal
cc_norm1	**0.65**	9.68	**0.02**	34.11	22.85	3.32
cc_norm2	31.79	3.95	82.45	19.15	21.65	1.26
cc_norm3	**0.02**	**0.37**	**0.02**	57.99	75.13	55.65
cc_norm4	62.97	3.17	100.00	2.26	52.62	1.58
lifetime	16.83	73.98	2.45	24.06	12.83	0.37
In	**0.00**	**0.01**	**0.00**	17.68	97.47	12.83
tau	3.27	**0.65**	12.05	24.06	28.13	1.77

The ranksum test clearly suggests that only the cancer group can be potentially distinguished from the other classes; thus, all the other classes were combined into a

non-cancer group. The ranksum test was again performed on these two groups. The results are described in the Table 5 below.

Table 5 “p” in percentage from Ranksum Test between cancer data and non-cancer data

	Channel 1	Channel 2	Channel 3
	Cancer-noncancer	Cancer-noncancer	Cancer-noncancer
cc_norm1	18.65	**0.84**	**0.04**
cc_norm2	**0.00**	**0.00**	21.26
cc_norm3	25.97	**0.08**	**0.00**
cc_norm4	**0.00**	**0.01**	35.09
lifetime	**0.00**	**0.00**	7.45
In	**0.00**	1.19	**0.00**
tau	**0.00**	**0.00**	**0.96**

According to the results of the ranksum test, only 15 features showed significant difference ($p < 1\%$) between the non-cancer and cancer groups, which are cc_norm2, cc_norm4, lifetime, normalized intensity, and tau in channel 1; cc_norm1, cc_norm2, cc_norm3, cc_norm4, lifetime, and tau in channel 2; cc_norm1, cc_norm3, normalized intensity, and tau in channel 3.

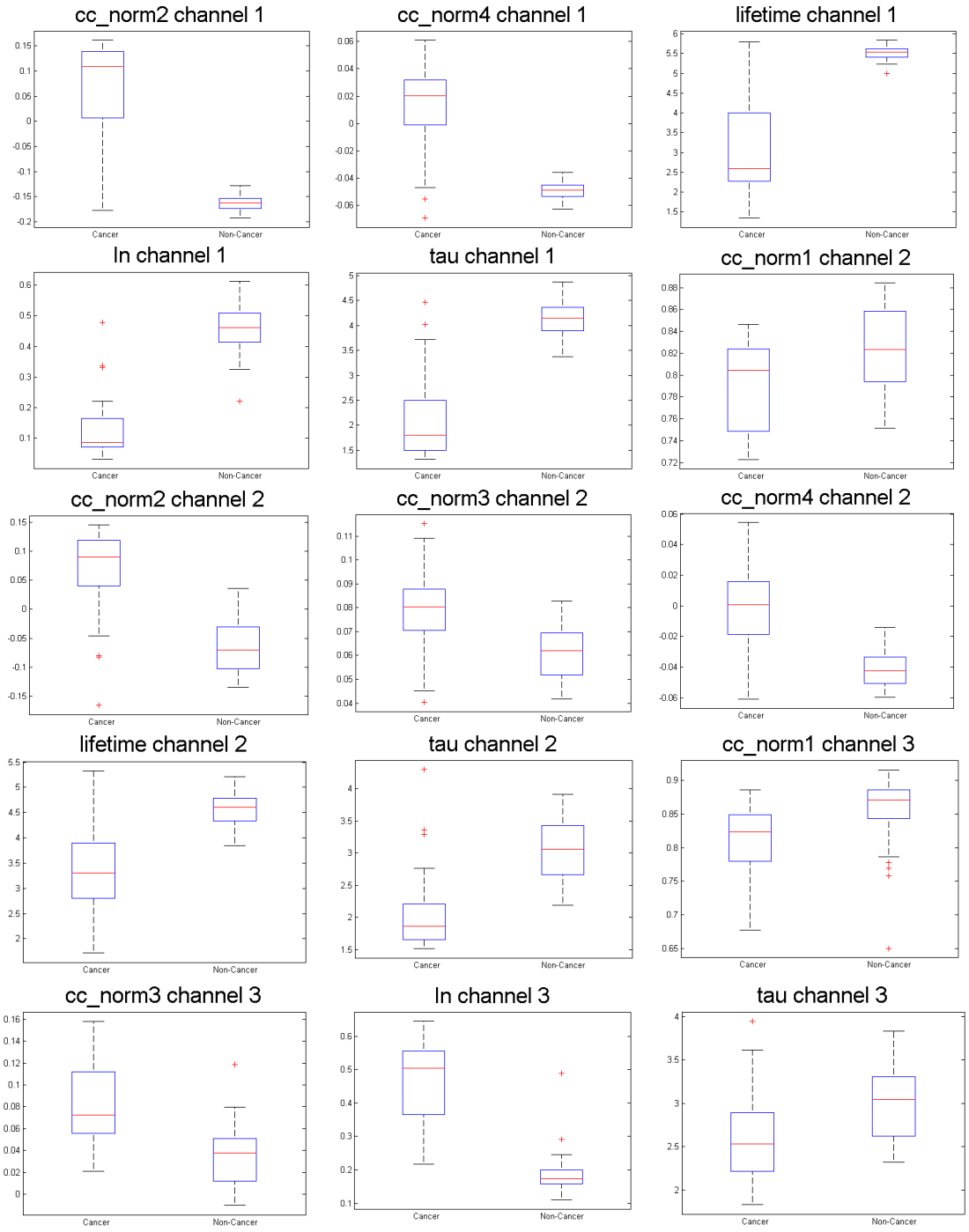

Figure 5 Boxplot of cancer and non-cancer data distribution with 15 features selected from ranksum test

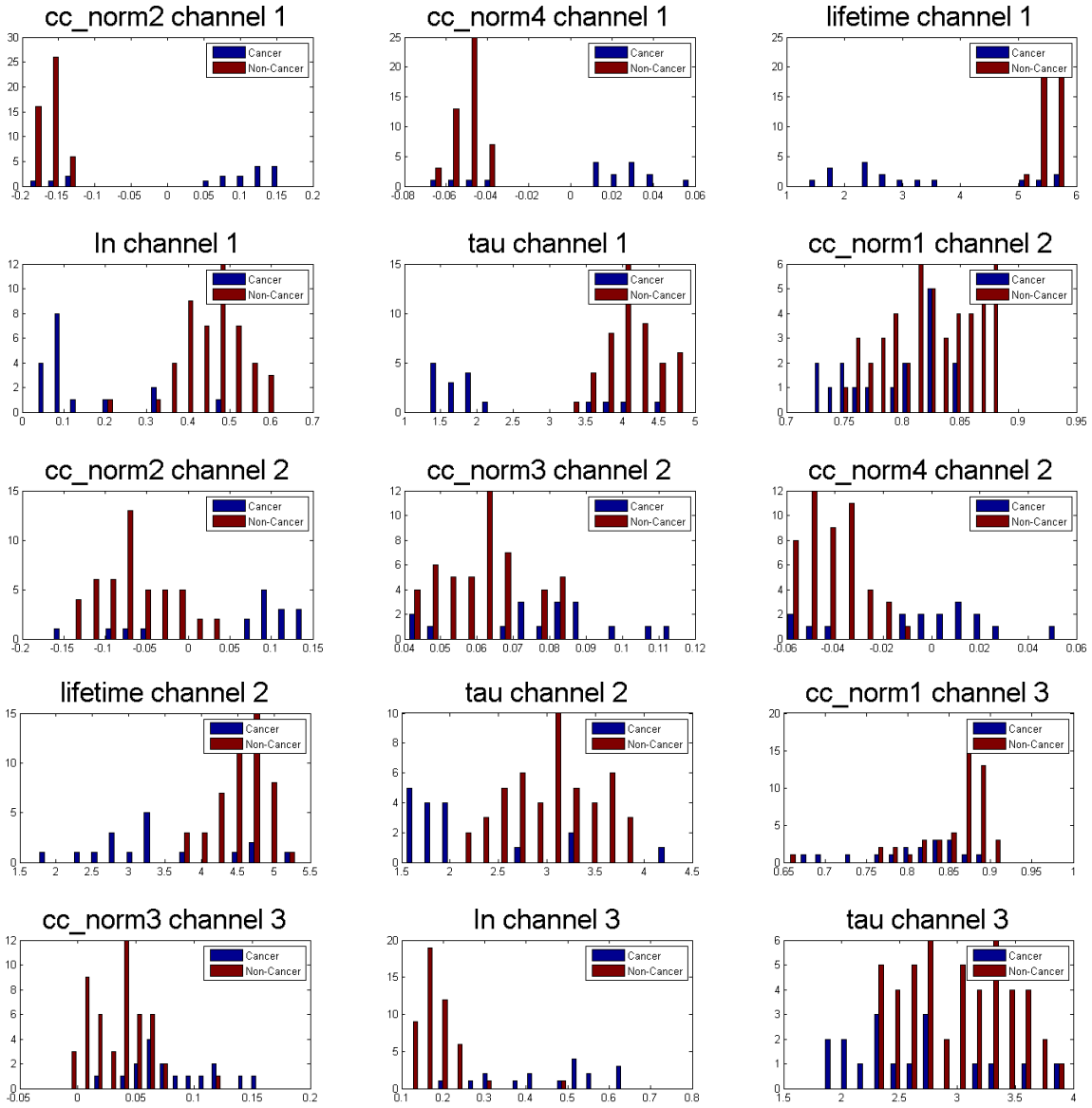

Figure 6 Histogram of cancer and non-cancer data distribution with 15 features selected from ranksum test.

After examining the p-values of the ranksum test, we also looked at both the boxplot (Figure 5) and the histograms (Figure 6) of each feature to gain some insight

about their underlying distributions. Based on these, we further discarded the following features: cc_norm1 in channel 2; cc_norm1, cc_norm3, and tau in channel 3. As a result, only 11 features were remaining: cc_norm2, cc_norm4, lifetime, normalized intensity, and tau in channel 1; cc_norm2, cc_norm3, cc_norm4, lifetime, and tau in channel 2; normalized intensity in channel 3.

3.3 Classifier Settings with Corresponding Performance

The Sequential Floating Forward Selection algorithm was carried out. Initially, the algorithm was carried out on the remaining 11 features selected out of the statistical analysis. The results are summarized in Tables 7-8 and Figures 7-10. In the table, each step comprises of two columns. The left column represents the error rate assuming the inclusion of the new feature whereas the right column represents the error rate assuming the exclusion of the current feature. In addition, note that the last step is purposely omitted in the tables below since it will not bring any changes to the recommended feature set. In each step, the suggested features are highlighted in bold. As delineated in Figure 3, selected feature set changes in a way that lowers the error rate the most. The two most bottom rows shows the confusion matrices with feature set chosen by the corresponding step.

Table 6 Error rate for 1-Nearest-Neighbor method

1NN		Step 1		Step 2		Step 3	
cc_norm2_ch1		0.137	N/A	0.108	N/A	0.083	N/A
cc_norm4_ch1		0.161	N/A	0.112	N/A	0.083	N/A
lifetime_ch1		0.135	N/A	0.119	N/A	0.090	N/A
In_ch1		0.118	N/A	0.098	N/A	0.083	N/A
tau_ch1		0.718	N/A	0.111	N/A	0.091	N/A
cc_norm2_ch2		0.171	N/A	0.087	N/A	0.081	N/A
cc_norm3_ch2		0.298	N/A	0.102	N/A	0.081	N/A
cc_norm4_ch2		0.207	N/A	0.101	N/A	**0.078**	0.080
lifetime_ch2		0.190	N/A	0.098	N/A	0.089	N/A
tau_ch2		0.627	N/A	**0.080**	0.114	**N/A**	0.101
In_ch3		**0.114**	N/A	**N/A**	0.627	**N/A**	0.194
TN	FP	5342	466	5424	384	5445	363
FN	TP	432	1625	246	1811	250	1807

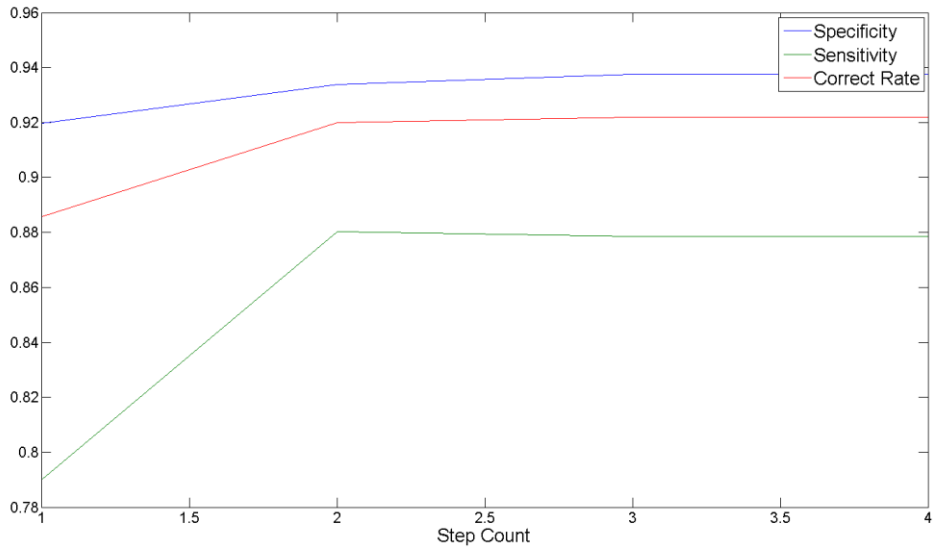

Figure 7 The flow of changes on specificity, sensitivity, and correct rate for 1NN

Table 7 Error rate for 3-Nearest-Neighborhood method

3NN		Step 1		Step 2	
cc_norm2_ch1		0.101	N/A	0.101	N/A
cc_norm4_ch1		0.114	N/A	0.101	N/A
lifetime_ch1		0.100	N/A	0.116	N/A
In_ch1		0.094	N/A	0.094	N/A
tau_ch1		0.649	N/A	0.107	N/A
cc_norm2_ch2		0.130	N/A	0.083	N/A
cc_norm3_ch2		0.246	N/A	0.090	N/A
cc_norm4_ch2		0.165	N/A	0.091	N/A
lifetime_ch2		0.142	N/A	0.094	N/A
tau_ch2		0.613	N/A	**0.078**	0.094
In_ch3		**0.094**	N/A	**N/A**	0.613
TN	FP	5460	348	5457	351
FN	TP	389	1668	262	1795

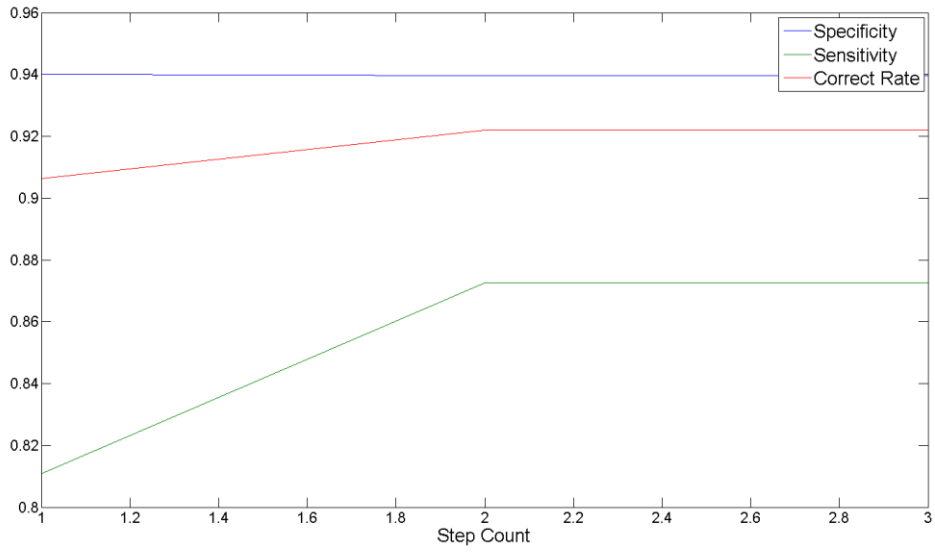

Figure 8 The flow of changes on specificity, sensitivity, and correct rate for 3NN

Table 8 Error rate for 5-Nearest-Neighborhood method

5NN		Step 1		Step 2		Step 3		Step 4		Step 5	
cc_norm2_ch1		0.091	N/A	0.100	N/A	0.081	N/A	0.078	N/A	0.078	N/A
cc_norm4_ch1		0.102	N/A	0.099	N/A	0.082	N/A	0.078	N/A	**0.077**	0.078
lifetime_ch1		0.088	N/A	0.113	N/A	**0.078**	0.081	**0.000**	0.082	**N/A**	0.083
In_ch1		0.092	N/A	0.091	N/A	0.079	N/A	0.081	N/A	0.081	N/A
tau_ch1		0.628	N/A	0.102	N/A	0.081	N/A	0.078	N/A	0.079	N/A
cc_norm2_ch2		0.120	N/A	0.083	N/A	0.080	N/A	0.078	N/A	0.078	N/A
cc_norm3_ch2		0.227	N/A	0.085	N/A	0.082	N/A	**0.078**	0.078	**N/A**	0.078
cc_norm4_ch2		0.149	N/A	0.090	N/A	0.080	N/A	0.079	N/A	0.078	N/A
lifetime_ch2		0.126	N/A	0.094	N/A	0.079	N/A	0.079	N/A	0.079	N/A
tau_ch2		0.592	N/A	**0.081**	0.088	**N/A**	0.113	**N/A**	0.110	**N/A**	0.112
In_ch3		**0.088**	**N/A**	**N/A**	0.592	**N/A**	0.084	**N/A**	0.084	**N/A**	0.084
TN	FP	5492	316	5451	357	5716	92	5719	89	5720	88
FN	TP	379	1678	278	1779	523	1534	522	1535	521	1536

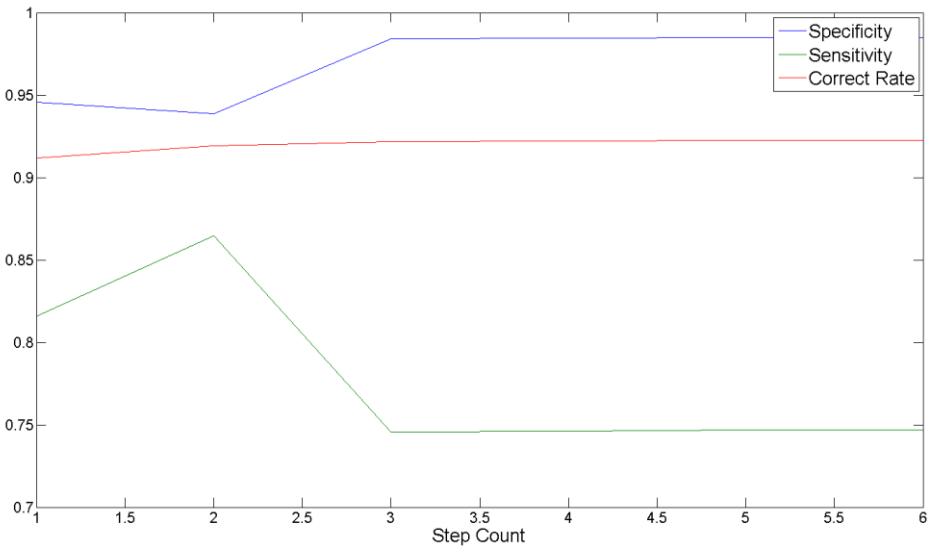

Figure 9 The flow of changes on specificity, sensitivity, and correct rate for 5NN

Table 9 Error rate for 7-Nearest-Neighborhood method

7NN		Step 1		Step 2		Step 3		Step 4		Step 5		Step 6	
cc_norm2_ch1		**0.085**	N/A	**N/A**	0.593	**N/A**	0.082	**N/A**	0.077	**N/A**	**0.076**	0.076	N/A
cc_norm4_ch1		0.098	N/A	0.083	N/A	0.080	N/A	0.081	N/A	0.076	N/A	**0.076**	0.076
lifetime_ch1		0.089	N/A	0.084	N/A	0.082	N/A	**0.077**	0.079	**N/A**	0.082	**N/A**	0.083
In_ch1		0.089	N/A	0.097	N/A	0.086	N/A	0.081	N/A	0.080	N/A	0.080	N/A
tau_ch1		0.617	N/A	0.084	N/A	0.087	N/A	0.082	N/A	0.077	N/A	0.077	N/A
cc_norm2_ch2		0.115	N/A	0.088	N/A	0.090	N/A	0.080	N/A	0.077	N/A	0.076	N/A
cc_norm3_ch2		0.219	N/A	0.083	N/A	0.081	N/A	0.080	N/A	**0.076**	0.077	**N/A**	0.076
cc_norm4_ch2		0.144	N/A	0.090	N/A	0.079	N/A	0.079	N/A	0.077	N/A	0.076	N/A
lifetime_ch2		0.123	N/A	0.094	N/A	0.092	N/A	0.078	N/A	0.077	N/A	0.078	N/A
tau_ch2		0.593	N/A	**0.080**	0.085	**N/A**	0.098	**N/A**	0.106	**N/A**	0.108	**N/A**	0.109
In_ch3		0.087	N/A	0.098	N/A	**0.079**	0.080	**N/A**	0.082	**N/A**	0.083	**N/A**	0.081
TN	FP	5683	125	5720	88	5506	302	5740	68	5743	65	5744	64
FN	TP	542	1515	541	1516	322	1735	534	1523	532	1525	533	1524

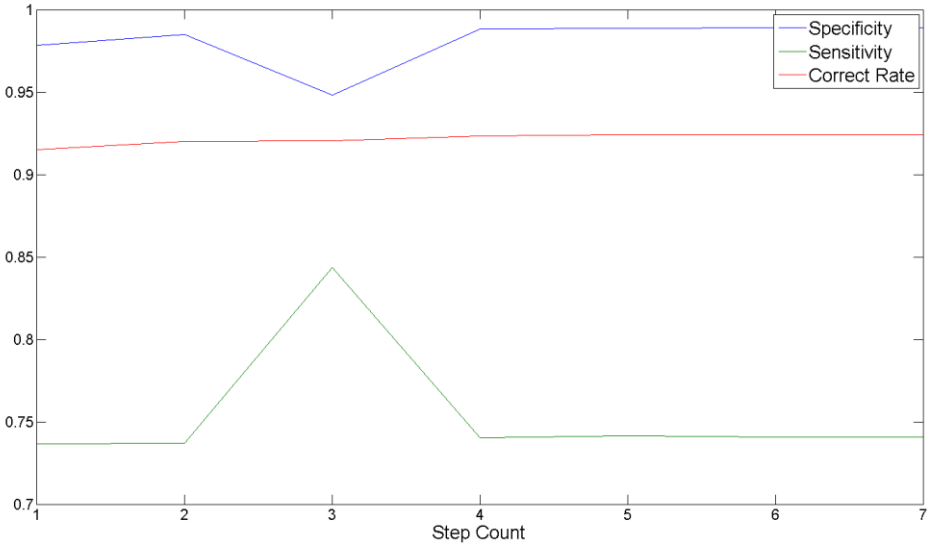

Figure 10 The flow of changes on specificity, sensitivity, and correct rate for 7NN

Considering both error rate and sensitivity, classifiers with various Ks shows similar performances with suggested feature set. Furthermore, as K gets lower, the performance tends to slightly move towards sensitivity whereas the performance tends to shift towards specificity as K gets higher. More specifically, 1NN can cause over-fitting due to the high sensitivity whereas low sensitivity can be an issue for high K. Good compromise is indeed on demand in this case. As a result, 3NN will be implemented. Furthermore, the sequential floating forward search algorithm suggests utilize $\frac{1}{e}$ lifetime in channel 2 and normalized intensity in channel 3 with 3NN. The resulting correct rate, specificity, and sensitivity for detecting cancerous were 92.2%, 94.0%, and 87.3%, respectively.

3.4 Tissue Classification

At this point, all the parameters that need to be determined in order to build an optimal classifier have been found. Now, 3-Nearest-Neighborhood classifier with $\frac{1}{e}$ lifetime in channel 2 and normalized intensity in channel 3 can classify the whole regions from seven tissues, and the results are described below from Figure 11-17. Note that the Classification Map on the left shows cancer region as black and non-cancer region as white. A photograph of the imaged tissue is also provided on the right as a reference. In addition, the ROIs used to train the classifier are marked with 11×11 pixel squares; blue for the non-cancerous and red for the cancerous ROI.

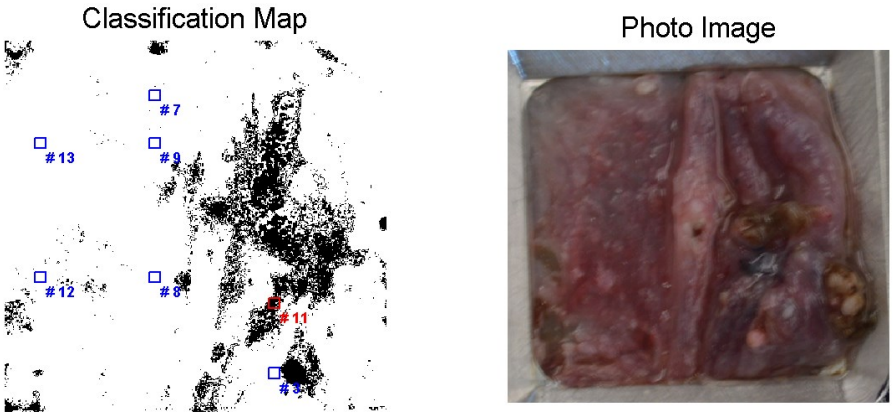

Figure 11 Results of the classification and the actual tissue image of the tissue #1

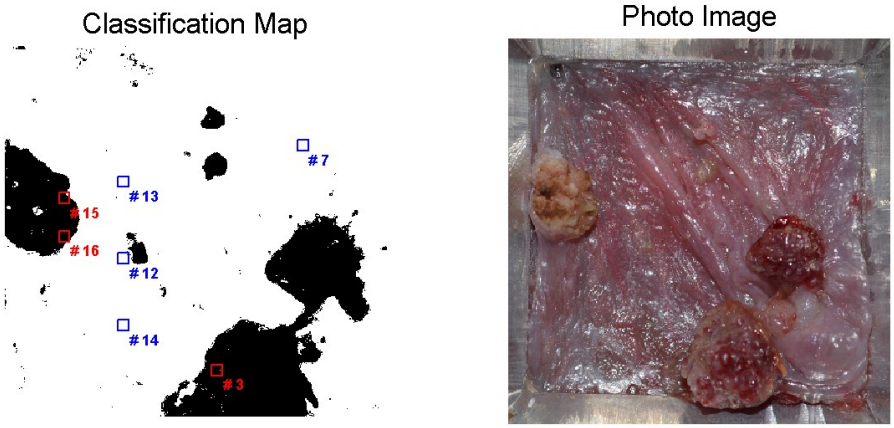

Figure 12 Results of the classification and the actual tissue image of the tissue #2

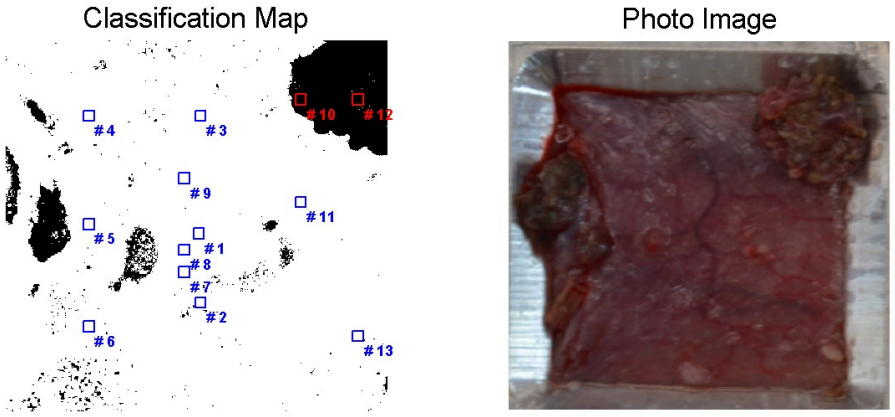

Figure 13 Results of the classification and the actual tissue image of the tissue #3

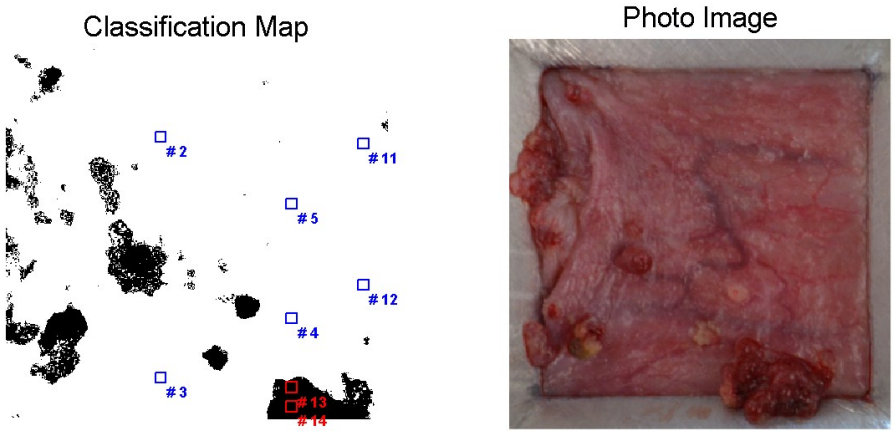

Figure 14 Results of the classification and the actual tissue image of the tissue #4

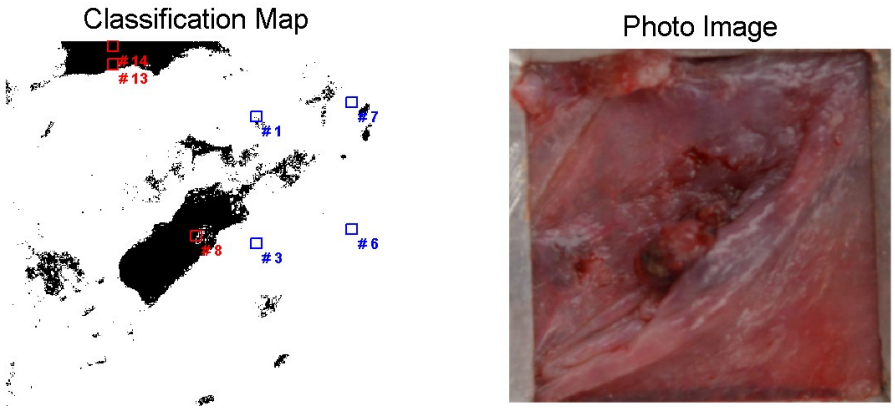

Figure 15 Results of the classification and the actual tissue image of the tissue #5

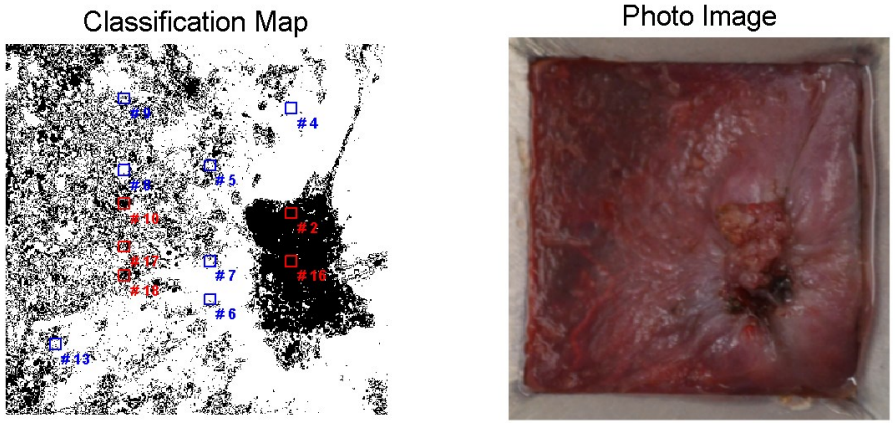

Figure 16 Results of the classification and the actual tissue image of the tissue #6

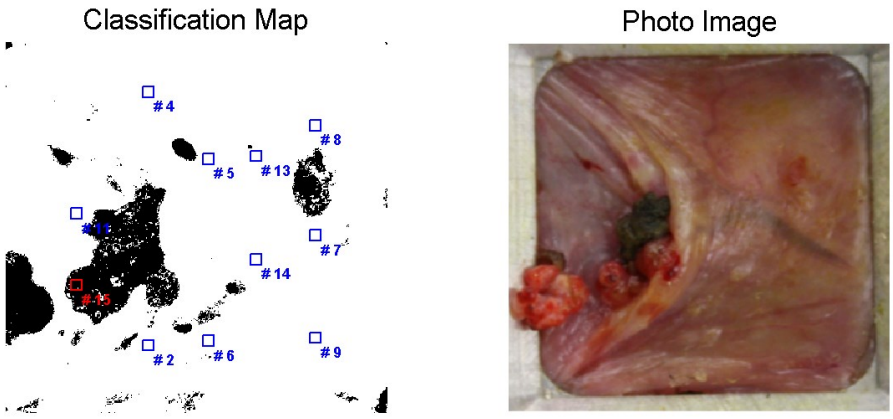

Figure 17 Results of the classification and the actual tissue image of the tissue #7

CHAPTER IV

DISCUSSION

In this study, all the features except normalized intensity are derived from the impulse response function (IRF), which is estimated from the Laguerre deconvolution algorithm. It is therefore, obvious that the accuracy of the deconvolution algorithm plays a major role in determining the performance of the classifier.

Currently, the algorithm implements the global alpha that minimizes the global error which is defined as the mean square error of the estimated IRF [26]. However, the alpha reflects the decay rate of the Laguerre function as can be noticed from Figure 18. Specifically, larger alpha creates slow decay and vice versa. For example, if fluorophores with a short lifetime dominates the tissue, global alpha will be low. However, if there is a small region where the fluorophores of high lifetime dominate, the IRF in this region may not be estimated accurately. Obviously, multiple alphas can be a solution to solve such problem. Segmenting the image based on the FLIM curve and assigning different optimal alpha to each of the segmented regions may be one way to improve the algorithm.

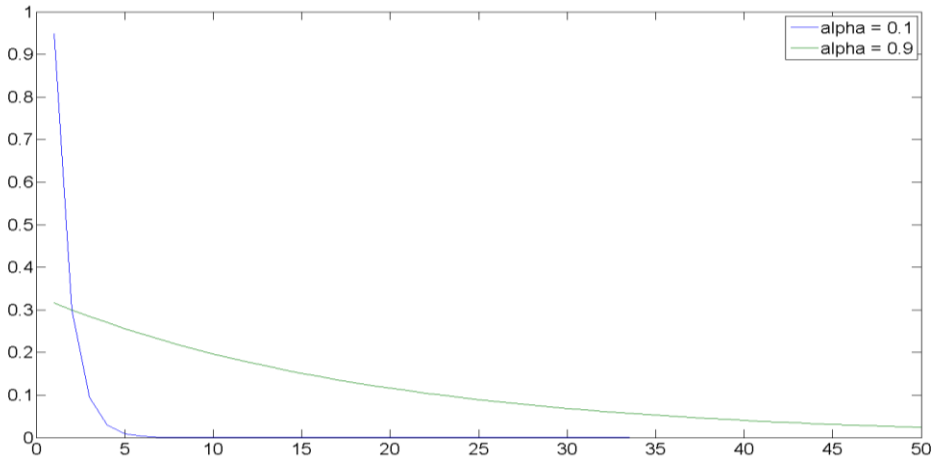

Figure 18 First-order Laguerre function with different alpha and unit coefficient

As the dimensionality of the features increases, the volume of the feature space increases as well as the sparsity of the data. The sparse data can be problematic since the models are built through learning, and it is valid only in the area where the learning data are available [28]. With every other constraints unchanged, the size of the required data grows exponentially with the dimension [28]. For example, if 10 data points seem reasonable to develop a reliable 1-dimensional model, 100 data points are necessary to train a 2-dimensional model with the same reliability [28]. As a result, both the large size of the data and the low dimensionality are desirable in developing reliable classification algorithm. In most circumstances, the size of the data is limited, and therefore the dimensionality should be kept low for low sparsity [28]. In this study, the feature dimensionality has been reduced through two different steps: statistical analysis and

feature selection algorithm. At the end, the optimal features included both lifetime parameter and the intensity parameter, and it validated the advantage of using FLIM.

As presented in section 3.2, 3NN with its selected feature set (tau_ch2, In_ch3) has shown decent performance. However, it turns out that most of the misclassification has occurred in the data from one of the hamster (tissue #6).

The exceptional behavior of the data from tissue #6 can be seen more clearly from the confusion matrix. Equation 6 illustrates how much hamster tissue #6 contributes to the overall misclassification. The 6th matrix in equation 6 corresponds to the 6th cross-validation, which uses the data from hamster tissue #6 as test set whereas all the other data are used as training set. It can be calculated that approximately 87.5% of the false positive and approximately 76.0% of the false negative has come from the tissue #6 data.

$$\begin{bmatrix}719 & 7\\ 42 & 79\end{bmatrix}+\begin{bmatrix}482 & 2\\ 18 & 345\end{bmatrix}+\begin{bmatrix}1331 & 0\\ 0 & 242\end{bmatrix}+\begin{bmatrix}726 & 0\\ 0 & 242\end{bmatrix}+\begin{bmatrix}449 & 35\\ 3 & 360\end{bmatrix}+$$

$$\begin{bmatrix}540 & 307\\ 199 & 406\end{bmatrix}+\begin{bmatrix}1210 & 0\\ 0 & 121\end{bmatrix}=\begin{bmatrix}5457 & 351\\ 262 & 1795\end{bmatrix} \quad (6)$$

Without tissue #6, the feature selection algorithm suggested cc_norm2 in the channel 1and normalized intensity in the channel 1 as the best features for 3NN. The performance of this classifier is illustrated as a confusion matrix in equation 7.

$$\begin{bmatrix}4922 & 39\\ 34 & 1418\end{bmatrix} \quad (7)$$

The performance of this classifier looks extremely promising. Its correct rate, specificity, and sensitivity for detecting cancer lesions were 98.9%, 99.2%, and 97.7%, respectively. The rate of misclassification for the ROIs of tissue #6 can partially be

explained in terms of its unique histopathological characteristics. More specifically, ROI #10, #17, #18 in tissue #6 show comparatively thin epithelium. Though these three ROIs were all labeled as high-graded-dysplasia (HGD) the epithelial layers on these ROIs are much thinner compared to the HGD ROIs in the other animals.

Although many lesions were clearly distinguishable based on visual inspection, some of them were not. As an example, the classification map shown in Figure 19 highlighted several cancerous regions (marked by red circles) that were not obvious by visual inspection. These are promising results in that the proposed 3NN classifier can help clinician more accurately detect the oral cancer than by visual inspection only.

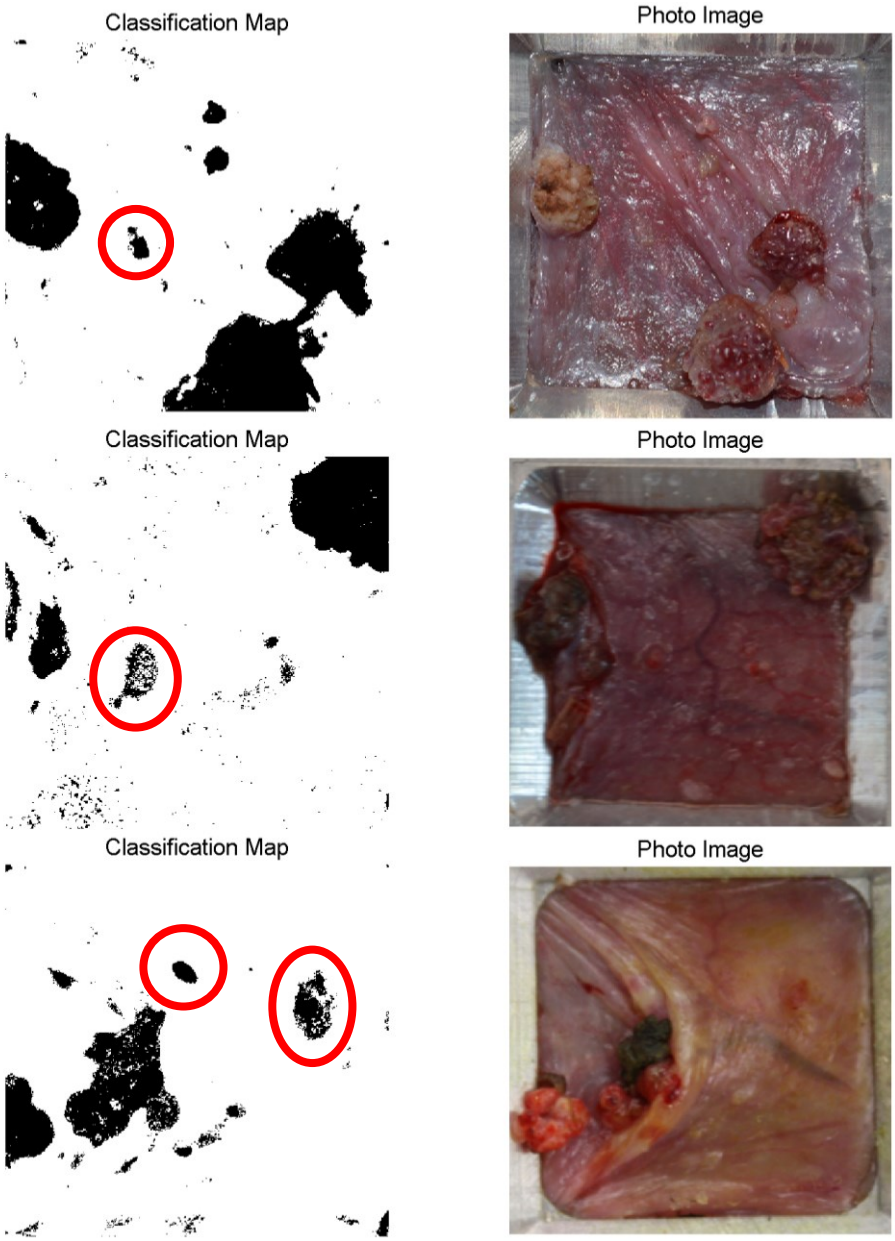

Figure 19 Various precancerous lesions which are not revealed from visual inspection

CHAPTER V

CONCLUSION

In this study, the clinical potential of the endogenous multispectral Fluorescence lifetime imaging microscopy (FLIM) was investigated to objectively detect oral cancer. To this end, *in vivo* FLIM imaging was performed on a hamster cheek pouch model with an oral epithelial cancer. The autofluorescence emissions of the hamster tissue were recorded in three different spectral bands which were determined based on the peak emission wavelength of three major fluorophores of hamster mucosal tissue: collagen (390±20 nm), NADH (452±22.5 nm), and FAD (>500 nm). Then, a total of 7 features pertaining to FLIM were extracted from each channel, providing 21 features overall. To design a classifier in a supervised approach, a training set is required, in which each pixel is labeled with one of the four groups. In this study, we utilized a total of 65 regions of interest (ROI) from the imaged cheek pouch of seven hamsters, for which the histopathological diagnosis could be correlated. The resulting database was used to train a K-Nearest-Neighborhood (KNN) algorithm aimed to detect benign from pre-malignant/malignant lesions. In addition, a Sequential Floating Forward Selection (SFFS) was applied to optimize the KNN algorithm and identify a subset of features that would maximize the classification performance.

The best performance corresponded to the 3-NN algorithm with the $\frac{1}{e}$ lifetime in the NADH channel and the normalized intensity in FAD channel as features. The overall accuracy, sensitivity and specificity for detecting pre-malignant and malignant lesions

were 92.2%, 87.3%, and 94%, respectively, assessed using a cross-validation method. It has to be noted that the feature selection algorithm suggested both lifetime parameter and intensity parameter for an optimal feature set, which validates the need to utilize endogenous FLIM for the objective detection of oral cancer. At last, all data from the 65 ROIs were used to train the 3NN classifier to classify the full tissue areas.

These results suggest that multispectral endogenous FLIM has a potential to screen malignant oral epithelial tissue. This technology, however, still needs to be evaluated in human patients.

REFERENCES

[1] I. Pavlova, M. Pavlova, A. Williams, R. El Naggar and A. Richards Kortum. Understanding the biological basis of autofluorescence imaging for oral cancer detection: High-resolution fluorescence microscopy in viable tissue. *Clinical Cancer Research 14(8),* pp. 2396-2404. 2008. DOI: 10.1158/1078-0432.CCR-07-1609.

[2] C. Poh, D. MacAulay, P. Laronde, L. Michele Williams and M. Zhang. Squamous cell carcinoma and precursor lesions: Diagnosis and screening in a technical era. *Periodontol. 2000 57(1),* pp. 73-88. 2011. DOI: 10.1111/j.1600-0757.2011.00386.x.

[3] M. Lingen, J. Lingen, T. Kalmar and P. Karrison. Critical evaluation of diagnostic aids for the detection of oral cancer. *Oral Oncol. 44(1),* pp. 10-22. 2008. DOI: 10.1016/j.oraloncology.2007.06.011.

[4] R. Mehrotra and D. Mehrotra. Exciting new advances in oral cancer diagnosis: Avenues to early detection. *Head & Neck Oncology 3(1),* pp. 33. 2011. DOI: 10.1186/1758-3284-3-33.

[5] K. H. Awan, P. R. Awan and S. Morgan. Evaluation of an autofluorescence based imaging system (VELscopeâ„¢) in the detection of oral potentially malignant disorders and benign keratoses. *Oral Oncol. 47(4),* pp. 274-277. 2011.

[6] M. Scheer, J. Scheer, A. Neugebauer, J. Derman, U. Fuss and J. Drebber. Autofluorescence imaging of potentially malignant mucosa lesions. *Oral Surgery, Oral Medicine, Oral Pathology, Oral Radiology and Endodontology 111(5),* pp. 568-577. 2011. DOI: 10.1016/j.tripleo.2010.12.010.

[7] K. McNamara, B. McNamara, E. Martin and J. Evans. The role of direct visual fluorescent examination (VELscope) in routine screening for potentially malignant oral mucosal lesions. *Oral Surgery, Oral Medicine, Oral Pathology and Oral Radiology 114(5),* pp. 636-643. 2012. DOI: 10.1016/j.oooo.2012.07.484.

[8] C. Farah, L. Farah, A. McIntosh and M. Georgiou. Efficacy of tissue autofluorescence imaging (velscope) in the visualization of oral mucosal lesions. *Head Neck 34(6),* pp. 856-862. 2012. DOI: 10.1002/hed.21834.

[9] P. Lane, M. Lane and C. Follen. Has fluorescence spectroscopy come of age? A case series of oral precancers and cancers using white light, fluorescent light at 405 nm, and reflected light at 545 nm using the trimira identafi 3000. *Gender Medicine 9(1),* pp. S25-S35. 2012. DOI: 10.1016/j.genm.2011.09.031.

[10] F. Koch, M. Koch, S. Kunkel and W. Biesterfeld. Diagnostic efficiency of differentiating small cancerous and precancerous lesions using mucosal brush smears

of the oral cavity-a prospective and blinded study. *Clin. Oral Investig. 15(5),* pp. 763-769. 2011.

[11] V. Bhoopathi, S. Bhoopathi and A. Kabani. Low positive predictive value of the oral brush biopsy in detecting dysplastic oral lesions. *Cancer 115(5),* pp. 1036-1040. 2009. DOI: 10.1002/cncr.24089.

[12] P. Guneri, J. B. Güneri, A. Epstein, A. Kaya, A. Veral and H. Kazandı. The utility of toluidine blue staining and brush cytology as adjuncts in clinical examination of suspicious oral mucosal lesions. *International Journal of Oral & Maxillofacial Surgery 40(2),* pp. 155-161. 2011 DOI: 10.1016/j.ijom.2010.10.022.

[13] G. P. Epstein J, The adjunctive role of toluidine blue in detection of oral premalignant and malignant lesions. *Current Opinion in Otolaryngology & Head & Neck Surgery, (17)*, pp. 79-87. 2009.

[14] N. Ramanujam. Fluorescence spectroscopy of neoplastic and non-neoplastic tissues. *Neoplasia 2(1-2),* pp. 89-117. 2000. DOI: 10.1038/sj.neo.7900077.

[15] I. Georgakoudi. NAD(P)H and collagen as in vivo quantitative fluorescent biomarkers of epithelial precancerous changes. *Cancer Res. 62(3),* pp. 682-687. 2002.

[16] Y. Wu and J. Wu. Autofluorescence spectroscopy of epithelial tissues. *J. Biomed. Opt. 11(5),* pp. 054023. 2006. DOI: 10.1117/1.2362741.

[17] J. Jabbour, S. Jabbour, B. Cheng, R. Malik, J. Cuenca, J. Jo, Y. Wright and K. Cheng. Fluorescence lifetime imaging and reflectance confocal microscopy for multiscale imaging of oral precancer. *J. Biomed. Opt. 18(4),* pp. 046012. 2013. . DOI: 10.1117/1.JBO.18.4.046012.

[18] Q. Fang, T. Fang, J. Papaioannou, R. Jo, K. Vaitha and L. Shastry. Time-domain laser-induced fluorescence spectroscopy apparatus for clinical diagnostics. *Rev. Sci. Instrum. 75(1),* pp. 151-162. 2004. DOI: 10.1063/1.1634354.

[19] C. Chang. Fluorescence lifetime imaging microscopy. *Methods Cell Biol. 81*pp. 495-524. 2007. DOI: 10.1016/S0091-679X(06)81024-1.

[20] A. Dabir, C. Dabir, Y. Trivedi, P. Ryu and J. Pande. Fully automated deconvolution method for on-line analysis of time-resolved fluorescence spectroscopy data based on an iterative laguerre expansion technique. *J. Biomed. Opt. 14(2),* pp. 024030. 2009. DOI: 10.1117/1.3103342.

[21] C. Morgan. Fluorescence lifetime imaging: An emerging technique in fluorescence microscopy. *Chromosome Research 4(4),* pp. 261-263. 1996. DOI: 10.1007/BF02263674.

[22] M. C. Skala, K. M. Skala, A. Riching, J. Gendron Fitzpatrick, K. W. Eickhoff, J. G. Eliceiri and N. White. In vivo multiphoton microscopy of NADH and FAD redox states, fluorescence lifetimes, and cellular morphology in precancerous epithelia. *Proc. Natl. Acad. Sci. U. S. A. 104(49),* pp. 19494-19499. 2007. DOI: 10.1073/pnas.0708425104.

[23] J. Lakowicz, *Principles of Fluorescence Spectroscopy.* New York: Springer, 2006.

[24] V. K. Ramanujan, J. Ramanujan, E. Zhang and B. Biener. Multiphoton fluorescence lifetime contrast in deep tissue imaging: Prospects in redox imaging and disease diagnosis. *J. Biomed. Opt. 10(5),* pp. 051407. 2005. DOI: 10.1117/1.2098753.

[25] J. A. Jo, L. Jo and Marcu. Ultrafast method for the analysis of fluorescence lifetime imaging microscopy data based on the laguerre expansion technique. *IEEE Journal of Selected Topics in Quantum Electronics 11(4),* pp. 835-845. 2005. DOI: 10.1109/JSTQE.2005.857685.

[26] P. Pande and J. Pande. Automated analysis of fluorescence lifetime imaging microscopy (FLIM) data based on the laguerre deconvolution method. *IEEE Transactions on Biomedical Engineering 58(1),* pp. 172-181. 2011. DOI: 10.1109/TBME.2010.2084086.

[27] P. Pudil, F. J. Pudil, J. Ferri and J. Novovicova. Floating search methods for feature selection with nonmonotonic criterion functions. *Proceedings of the 12th IAPR International Conference on Pattern Recognition (Cat. no.94CH3440-5) 2*pp. 279-283. 1994. DOI: 10.1109/ICPR.1994.576920.

[28] M. Verleysen. The curse of dimensionality in data mining and time series prediction. *Lecture Notes in Computer Science 3512*pp. 758-770. 2005. DOI: 10.1007/11494669_93.